IOP PUBLISHING PHYSICS IN MEDICINE AND BIOLOGY

Phys. Med. Biol. **56** (2011) 5335–5354 doi:10.1088/0031-9155/56/16/017

Validation of 3D multimodality roadmapping in interventional neuroradiology

Daniel Ruijters, Robert Homan, Peter Mielekamp, Peter van de Haar and Drazenko Babic

Interventional X-Ray (iXR), Philips Healthcare, Best, The Netherlands

E-mail: danny.ruijters@philips.com

Received 29 December 2010, in final form 5 July 2011
Published 28 July 2011
Online at stacks.iop.org/PMB/56/5335

Abstract

Three-dimensional multimodality roadmapping is entering clinical routine utilization for neuro-vascular treatment. Its purpose is to navigate intra-arterial and intra-venous endovascular devices through complex vascular anatomy by fusing pre-operative computed tomography (CT) or magnetic resonance (MR) with the live fluoroscopy image. The fused image presents the real-time position of the intra-vascular devices together with the patient's 3D vascular morphology and its soft-tissue context. This paper investigates the effectiveness, accuracy, robustness and computation times of the described methods in order to assess their suitability for the intended clinical purpose: accurate interventional navigation. The mutual information-based 3D–3D registration proved to be of sub-voxel accuracy and yielded an average registration error of 0.515 mm and the live machine-based 2D–3D registration delivered an average error of less than 0.2 mm. The capture range of the image-based 3D–3D registration was investigated to characterize its robustness, and yielded an extent of 35 mm and 25° for >80% of the datasets for registration of 3D rotational angiography (3DRA) with CT, and 15 mm and 20° for >80% of the datasets for registration of 3DRA with MR data. The image-based 3D–3D registration could be computed within 8 s, while applying the machine-based 2D–3D registration only took 1.5 μs, which makes them very suitable for interventional use.

(Some figures in this article are in colour only in the electronic version)

1. Introduction

The fusion of pre-operative soft-tissue images such as magnetic resonance (MR) and computed tomography (CT) with intra-operative fluoroscopy images can aid neurovascular treatment by providing detailed 3D information regarding the vascular morphology and pathology. The fused image allows more accurate endovascular guidance during procedures such as aneurysm

coiling, stent deployment and arteriovenous malformation (AVM) embolization (Bullitt *et al* 1999). Another clear clinical benefit is the fact that the amount of harmful iodine contrast medium can be reduced, since the vascular lumen can be visualized based on the multimodal data without injecting additional contrast agent. Therefore, the risk of contrast-induced nephropathy can be reduced considerably. Especially for patients with severe kidney failure, this is of eminent importance.

Though the fusion of 3D multimodal data with fluoroscopy images has been investigated in research settings for more than a decade, it is only now entering routine use in neuro-vascular treatment. The clinical adoption has been previously hampered by insufficient accuracy and long computation times of the available registration algorithms and hardware solutions. Especially during the live navigation, sufficient frame rates and low latencies are essential. The developments of powerful hardware and registration algorithms that can harvest this power have helped to overcome this hurdle. The common availability of 3D reconstruction in the cathlab and the presence of commercial solutions for multimodal roadmapping are other reasons that have enabled the adoption in clinical practice for patients with severe renal failure. The routine application of this technique demands that the accuracy, robustness, computation times and latencies of the applied techniques are investigated. The described methods have been implemented from scratch and are commercially available (XtraVision workstation, Philips Healthcare, Best, The Netherlands).

Registration is the process of spatially aligning two image datasets (which may originate from different modalities), such that the corresponding morphology in both datasets overlaps. Registration methods using stereotactic frames (see, e.g., Peters *et al* 1986) and other marker-based systems were already being developed in the 1980s. In the markerless domain, two fundamentally different approaches can be distinguished when projecting 3D volumetric data on 2D fluoroscopy images. In the first approach, called image-based registration, the registration process is driven by the image content. There are numerous image-based 2D–3D registration algorithms known in the literature for registering fluoroscopy images to either CT or MR images, e.g. Weese *et al* (1997), Kita *et al* (1998), Bullitt *et al* (1999), Penney *et al* (2001), Byrne *et al* (2004), van de Kraats *et al* (2005), Turgeon *et al* (2005), McLaughlin *et al* (2005), Tomaževič *et al* (2006), Jomier *et al* (2006), Groher *et al* (2007), Bender *et al* (2008). The image-based algorithms typically take a considerable amount of time to compute, ranging from a few seconds for methods that use a model of the anatomy of interest up to a few minutes for some intensity-driven approaches (McLaughlin *et al* 2005). Since these algorithms use the image content, sufficient landmark structures should be available in both images. In registration methods for angiographic applications, the structures are usually provided by filling the vasculature with harmful iodine contrast medium. Most registration methods are based on a single projection, which leads to a rather large registration error for the out-of-plane translation. As long as the projection angle does not change, this is not a big hurdle as it only leads to a slight mismatch in the magnification factor between the 2D and the 3D image (Groher *et al* 2007). When the C-arm is rotated, however, the out-of-plane translation error leads to a large shift between the 2D and the 3D image. This effect can be overcome by using two projection images at an angle of approximately 90° (Jomier *et al* 2006), but on a monoplane x-ray system this approach affects the clinical work flow and also doubles the amount of contrast medium and radiation.

The second approach is known as machine-based registration. With the introduction of motorized calibrated C-arm x-ray angiography, 3D reconstruction of the vasculature came within reach. Since such 3D rotational angiography (3DRA) datasets are obtained with the same apparatus as the 2D fluoroscopy data, it is possible to calculate a registration, based on the geometry pose (viewing incidence angles, source–detector distance (SID), etc), provided

that there was no patient motion between the acquisition of the 3DRA data and fluoroscopy data (Maintz and Viergever 1998, Kerrien *et al* 1998, Cañero *et al* 2002, Söderman *et al* 2005, Gorges *et al* 2005). This method also allows obtaining a registration, even when there are insufficient landmark structures present in the images, e.g. due to the absence of the iodine contrast medium in the fluoroscopy images (Baert *et al* 2004). A further advantage of machine-based registration is the fact that it can be computed in real time.

A method for determining the C-arm viewing incidence based on tracking a fiducial was proposed by Jain *et al* (2005), who reported a mean accuracy of 0.56 mm in translation (standard deviation $\sigma = 0.33$ mm) and 0.33° in rotation ($\sigma = 0.21°$), using a fiducial of size 3cm × 3cm × 5 cm. George *et al* (2011) have reported a registration error of less than 2.4 mm for fiducial-based registration of MRI with x-ray data. Here we present, however, a method that does not rely on fiducials, but only uses the sensor and calibration information concerning the geometry state provided by the C-arm system. By relying on the sensor-based projection of a 3DRA reconstruction on the 2D fluoroscopy image, the fusion of the multimodality data becomes a 3D–3D registration problem of intra- and preoperative data (which usually computes more accurately and robustly than 2D–3D registration). In an earlier work, we have described the fused visualization techniques in detail (Ruijters *et al* 2009). In this paper we intend to focus on the accuracy, robustness and computation speed aspects and their clinical implications.

2. Methods

2.1. Pre-interventional steps

Soft-tissue data, such as MR or CT, are often acquired for diagnostic purposes and/or treatment planning prior to the interventional treatment of neuro-vascular pathologies. Our goal is to integrate these data into a fused visualization during the treatment. In order to achieve this objective, a 3DRA dataset is obtained at the beginning of the intervention. Before the 3DRA and soft-tissue data can be fused with the live fluoroscopy image stream, a few pre-interventional steps have to be performed. In the first step, the 3DRA and soft-tissue dataset are registered, using an image-based registration algorithm.

Since we focus on cerebral applications, and there are only limited local deformations of the anatomical structures within the head, we can use a rigid registration (i.e. only a global translation and rotation). Rigid registration further has the property that it can be calculated relatively robustly and fast. Typically, a registration algorithm consists of a similarity measure, indicating the quality of a given spatial mapping, and an optimization algorithm, which searches the optimum of the similarity measure. The search space consists of the multi-dimensional control variables of the spatial mapping. We use mutual information as the similarity measure (Maes *et al* 1997), because it performs very well on inter-modality registration and does not demand any *a priori* knowledge of the datasets. In order to further limit the calculation time, we employ the Powell algorithm (Press *et al* 1992) as the optimizer, which is a so-called local optimizer. Local optimization algorithms are generally faster than global optimizers, but they do not guarantee that the overall optimum is found. To assure that the correct optimum is found, the image-based registration is preceded by an optional rough manual registration, which is to be performed by the clinician.

A multi-resolution approach is used to improve the capture range and the speed of the algorithm. First, the Powell optimizer is run with the 3DRA dataset downsampled to 64^3 voxels (Brigger *et al* 1999). The multimodal dataset is downsampled such that the voxel

Figure 1. Left: a slice out of a 3DRA dataset, showing the limited dynamic range. The visible anatomy are the sinuses, the skull and a contrast medium-filled aneurysm. Middle: a CT dataset, containing the facial structures. Right: a CT dataset, missing a major part of the facial structures, which hinders the registration process.

size in every direction matches the voxel size of the downsampled 3DRA data as closely as possible. Consequently the optimizer is run with the 3DRA data downsampled to 128^3 voxels and a matching multimodal dataset. The multimodal data is resampled to the grid of the 3DRA data using trilinear interpolation during the registration process.

Similar to Stancanello *et al* (2005), we use 256 gray level bins for the CT or MR dataset. The spatial resolution of a 3DRA reconstructions may be very high (a voxel can be as small as 0.1 mm), but they tend to have a rather poor signal-to-noise ratio (SNR). To reduce the sensitivity to noise we use a limited number (64) of gray level bins for the 3DRA dataset. As a result of the limited SNR, the vessels, bones and sinuses are the only structures that are well delineated, and can serve as landmark structures. The registration process is primarily determined by the facial structures, such as the eye sockets, the nose, the sinuses, etc. It is therefore of importance that such structures are contained both in the 3DRA dataset and the soft-tissue dataset, see figure 1. Also it is of importance that the spatial resolution of the soft-tissue dataset is sufficient. Especially the distance between the axial slices is too high in many datasets. To obtain registrations of sufficient accuracy, we requested it to be $\leqslant 2$ mm.

2.2. Registering 2D fluoroscopy to 3DRA data

The machine-based registration involves projecting the 3DRA data on the fluoroscopy images, based on the pose of the C-arm geometry. The x-ray C-arm system can rotate over three axes (see figure 2): rotation around the L-arm, rotation of the C-arm and angulation of the C-arm. The 3DRA dataset has to be rotated to match the orientation of the C-arm system. Let the origin of the coordinate system of the 3DRA data be positioned at the center of the dataset, and let the x-axis correspond to the short side of the table, the y-axis to the long side of the table and the z-axis point from the floor to the ceiling. The rotation of the detector coordinate system, with respect to the table can be expressed as

$$M = R_x \cdot R_y \cdot R_z. \tag{1}$$

Note that the order of the matrix multiplications is given by the mechanics of the C-arm system. The C-arm system's iso-center serves as the origin for the rotation matrices. The rotation of 3DRA volume to the detector coordinate system corresponds to the inverse of matrix M, which is equal to its transposed matrix M^T, since rotation matrices are orthogonal.

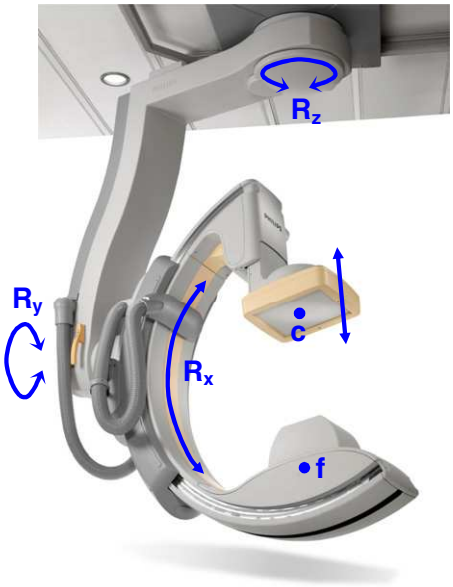

Figure 2. The x-ray angiography C-arm system's geometry, and its degrees of freedom. R_x corresponds to the angulation of the C-arm, R_y to the rotation, R_z is the L-arm rotation, f represents the focal spot and c is the center of the detector.

After rotating the 3DRA dataset into the appropriate orientation, the origin is translated from the iso-center to the detector center c. There still remains the task of projecting it with the proper perspective (see figure 3). The perspective matrix only depends on the x-ray SID. Using homogeneous coordinates it can be expressed as

$$P = \begin{pmatrix} \mathrm{SID} & 0 & 0 & 0 \\ 0 & \mathrm{SID} & 0 & 0 \\ 0 & 0 & 1 & 0 \\ 0 & 0 & -1 & \mathrm{SID} \end{pmatrix}. \tag{2}$$

The projection of 3DRA data on a fluoroscopy image by an ideal C-arm geometry has been described by Kerrien *et al* (1998). Their projection was divided into an extrinsic part, which described the geometry rotations and translations, and an intrinsic part describing the perspective projection by the x-ray source and detector. This subdivision originates from calibration procedures for optical cameras. The rotation axes of the real C-arm do not intersect and it suffers from systematic imperfections and mechanical bending, which motivated Cañero *et al* (2002) to introduce several increasingly sophisticated schemes for calibration of the extrinsic parameters for non-ideal geometries. Gorges *et al* (2005, 2006) refined the calibration procedure further by also taking the influence of the non-ideal geometry on the intrinsic parameters into account.

Our method resembles the approach of Gorges *et al* but does not make a subdivision between extrinsic and intrinsic parameters. For optical cameras this split makes sense, since the intrinsic parameters that describe the perspective projection are determined by the lens and the projection plane inside the camera housing, and therefore the intrinsic parameters are completely independent from the extrinsic ones. For non-ideal C-arm geometries, this is not

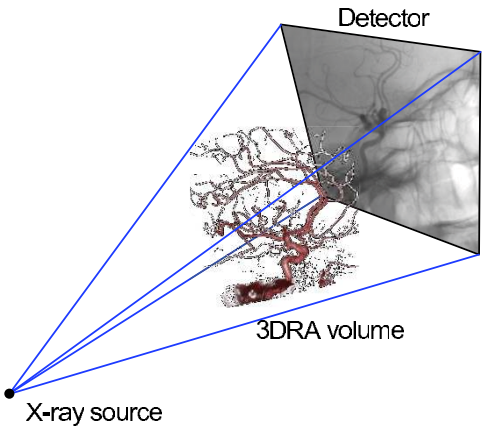

Figure 3. The virtual projection of a 3DRA dataset on a fluoroscopy image.

the case; the x-ray source and detector are mounted at opposite sides of the C-arm and the mechanical bending of the C-arm (affecting the intrinsic parameters) is dependent on its pose, which is described by the extrinsic parameters.

Since the rotation axes of the real C-arm do not intersect, there is no true iso-center. We define the point that has the smallest average distance to the rotation axes as our iso-center, and let the calibration procedure correct for the mechanical bending and the idealized model whereby the rotation axes intersect (as is assumed in equation (1)). Our calibration procedure is set up as follows: a dodecahedron phantom is placed approximately in the iso-center of the C-arm system. The regular dodecahedron has metal balls of fixed size at its corners. The metal balls are automatically detected in an x-ray projection image (figure 4). Due to the shape of the dodecahedron and the perspective in the projection image, there is only one pose that fits to the recognized balls, and therefore the exact position of the x-ray source and detector with respect to the dodecahedron can be determined by the direct linear transformation (DLT) algorithm (Hartley and Zisserman 2000). For each calibration angle the position of the x-ray source and detector are calculated from the sensor data that report the C-arm orientation and translation using an ideal model. The deviation of the real x-ray source and detector positions from their ideal counterparts is stored for every angle. The calibration positions are distributed at regular intervals of 20° in the range of [−30, 40] for the angulation angle R_x, and [−100, 100] for the rotation angle R_y.

The calibration procedure determines the true projection parameters for a number of projection angles evenly distributed over the hemisphere of possible C-arm locations for a fixed L-arm location (R_z) (Rougée *et al* 1993, Koppe *et al* 1995). Figure 5 illustrates the deviations of the focal spot position as a function of the rotation and angulation angles of the C-arm geometry that were found by the calibration of a particular C-arm system. For any position in between the calibrated positions, the deviations of the parameters are cubically averaged from the neighboring calibration data. Because the same dodecahedron calibration is used during the 3DRA reconstruction, the relation between the dodecahedron coordinate system and the 3DRA voxel coordinate system is known. As a result, a projection image taken from any chosen C-arm viewing incidence can be accurately mapped on the 3DRA dataset, using the calibration data.

Figure 4. A calibration image, showing the metal balls in the dodecahedron phantom. The crosses on top of the balls identify the successfully recognized balls. As can be seen from the image, ball numbers 15 and 19 were failed to identify properly (due to overlap). The white circles represent the back-projected dodecahedron corners after the dodecahedron was fitted to the image. The dodecahedron position in 3D space can even be determined when a few balls are missed.

3. Experimental evaluation

3.1. 2D–3D registration accuracy

The registration error that is present in the fused image can be decomposed into a part that can be contributed to the geometry-based 2D–3D registration and a part that is caused by the multimodality 3D–3D registration based on the mutual information criterion. The geometry-based registration uses cubic interpolation for parameter positions that are in between the calibrated positions. In order to quantify the misalignment that is associated with this method, we performed a full calibration of five C-arm x-ray angiography systems (Philips Allura, Best, The Netherlands) and obtained additionally images of the dodecahedron calibration phantom from nine viewing incidences in between the calibration positions. The interpolated parameter values were then compared to the parameter values delivered by fitting the dodecahedron to the observed images.

As can be seen in table 1, the average deviation of the detector center amounts to about 0.1 mm in the xy-plane, the displacement of the focal spot in the xy-plane is about 0.17 mm and the average rotational error is less than 0.1°. The average misalignment of the detector center and the focal spot in the z-direction is a bit larger (0.37 and 0.96 mm, respectively), but this contributes only to a slight error in the magnification due to the perspective in the image, and when these errors are expressed as a percentage of the SID (0.031% and 0.083%, respectively), it becomes apparent that they are truly negligible. Also it should be noted that these parameters are in the detector coordinate system. This means that when the C-arm is rotated, the larger absolute deviation in the z-direction is still perpendicular to the detector, and thus to the fluoroscopy image, which does not lead to any significant errors in the alignment.

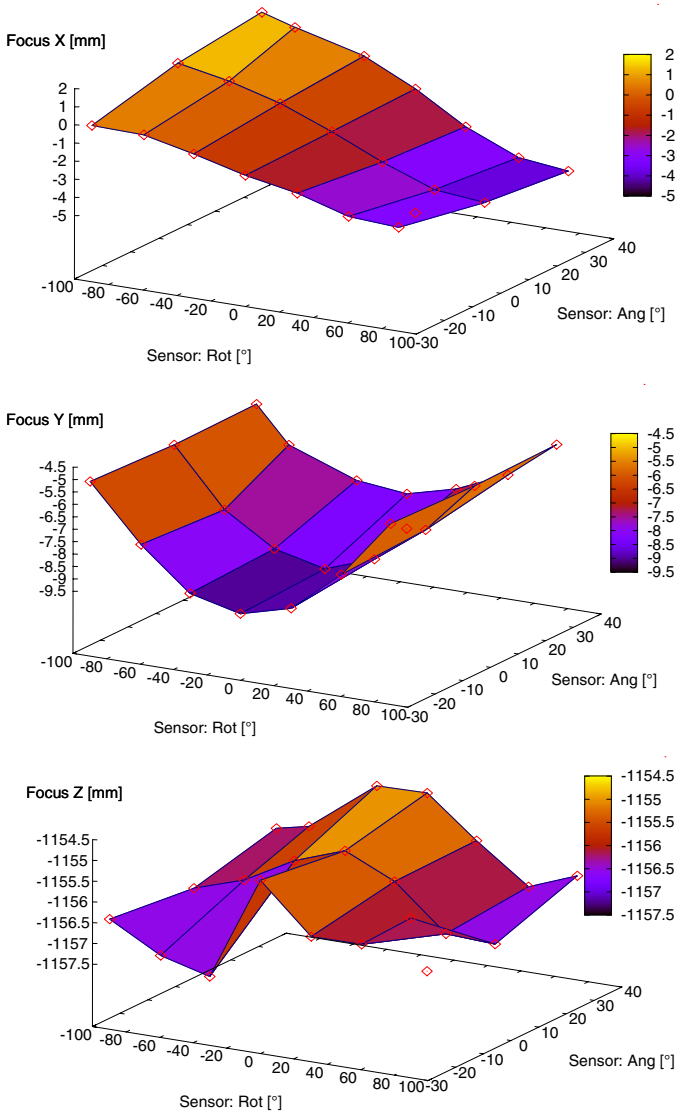

Figure 5. The calibration procedure with the dodecahedron phantom provides the real parameter values, which can be compared to the values provided by the geometry sensors. This figure illustrates the drifting of the focal spot position (one of the parameters) as a function of the C-arm rotation and angulation angles.

In order to assess to which extent certain sensor readings correspond to a reproducible position of the C-arm, predefined trajectories were repeated ten times while imaging the calibration dodecahedron. 100 images were acquired for each trajectory. The pose of the dodecahedron can be extracted from the resulting images by identifying the metal balls, just as is done during the calibration procedure. Figure 6 shows the results for a propeller trajectory (varying R_y while keeping all other parameters fixed) for the calculated iso-center in the x- and y-direction and the angulation angle, respectively. The average standard deviations

Table 1. The deviations (Δ) of the interpolated parameters versus the measured parameters using the dodecahedron phantom were established for five recently calibrated C-arm systems. This table reports the maximum, average and standard deviation for the delta of the rotation, angulation, L-arm angle, detector center position (in the xy-plane and the z-direction), and the focal spot position (in the xy-plane and the z-direction). The last column reports the absolute SID.

	Δ rot (deg)	Δ ang (deg)	Δ L-arm (deg)	Δ detector$_{xy}$ (mm)
Max	0.1276	0.2223	0.2216	0.2653
Average	0.0519	0.0776	0.0860	0.1023
SD	0.0432	0.0880	0.0724	0.0788
	Δ detector$_z$ (mm)	Δ foc$_{xy}$ (mm)	Δ foc$_z$ (mm)	SID (mm)
Max	0.8623	0.5625	2.7779	1189
Average	0.3656	0.1684	0.9629	1165
SD	0.2815	0.1451	0.8007	16.36

Table 2. Standard deviation of the C-arm position parameters, based on ten dodecahedron scans of 100 images each, averaged over all images. For the roll trajectory only the R_x angle is varied, whereas for the propeller trajectories only R_y is varied. The *Propeller1* trajectory was obtained with the detector in portrait mode and without C-arm motion between scans, the *Propeller2* trajectory was in the portrait mode with C-arm motion between the scans, and *Propeller3* was in the landscape mode with C-arm motion between the scans.

	Roll	Propeller1	Propeller2	Propeller3
iso-x (mm)	0.019	0.010	0.014	0.013
iso-y (mm)	0.024	0.0080	0.0092	0.0093
iso-z (mm)	0.079	0.058	0.070	0.077
rot (degrees)	0.028	0.054	0.025	0.045
ang (degrees)	0.0064	0.0048	0.0050	0.0053
larm (degrees)	0.0074	0.0058	0.0058	0.0062

for the various trajectories are presented in table 2. The variation in the observed C-arm poses is very small (less than 0.1 mm and 0.01°). Moving the C-arm between the trajectories only impacts the results minimally, as can be seen by comparing the results for *Propeller1*, *Propeller2* and *Propeller3* in table 2. There are several spikes in the graphs in figure 6. However, these correspond exactly to those images where the metal balls on the corners of the dodecahedron overlapped, which lead to miscalculations of the C-arm position. The deviation from the sensor information can amount to multiple millimeters, but proves to be very consistent and reproducible. Our results correspond well to those reported by Fahrig and Holdsworth (2000) for image-intensifier-based C-arm systems. Analogous to the advice of Fahrig and Holdsworth, the clinical systems are recalibrated every 6 months.

3.2. 3D–3D registration accuracy

To evaluate the registration misalignment due to the mutual information-based registration, we performed a 3DRA reconstruction and a cone-beam CT reconstruction using a soft-tissue protocol of a head phantom on the same C-arm system (figure 7). The soft-tissue protocol records six times more images (620 images versus 100 images for 3DRA) and performs extra corrections to reduce the influence of scatter and to improve the contrast resolution

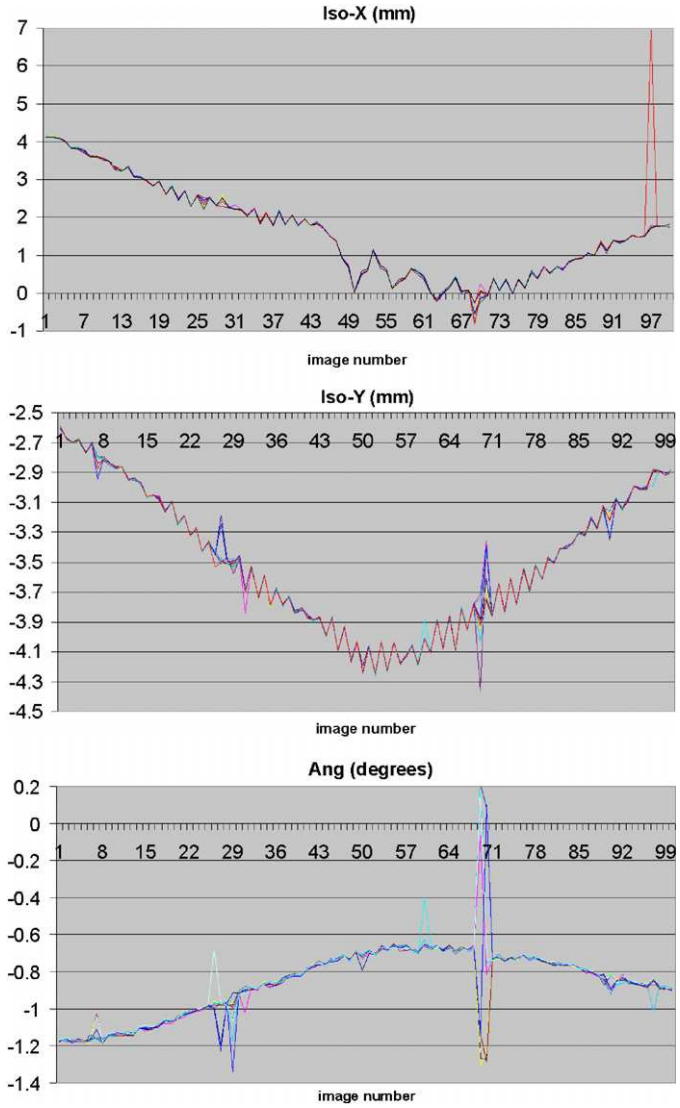

Figure 6. Plots of the deviation of the calculated iso-center and angulation position with respect to the sensor information, based on ten dodecahedron scans of 100 images each.

(Noordhoek *et al* 2006, Kalender and Kyriakou 2007), in order to deliver images that resemble multi-slice CT data. Because the datasets were obtained with the same equipment, the gold standard transformation matrix is known. The measurements were obtained from 295 registrations, initialized with random rigid transformation matrices (mean initial translation was 58.27 mm, $\sigma = 38.47$, min $= 5.20$, max $= 124.18$, mean initial rotation was 57.81°, $\sigma = 29.27$, min $= 5.19$, max $= 89.13$). The registration algorithm yielded on average an absolute residual translation error of 0.515 mm ($\sigma = 0.017$, min $= 0.495$, max $= 0.588$) and a mean absolute residual rotation error of 0.241° ($\sigma = 0.031$, min $= 0.180$, max $= 0.307$). The voxel size of the cone-beam CT dataset was 0.5 mm^3 and for the 3DRA it was 1 mm^3, which means that the registration algorithm delivered sub-voxel accuracy.

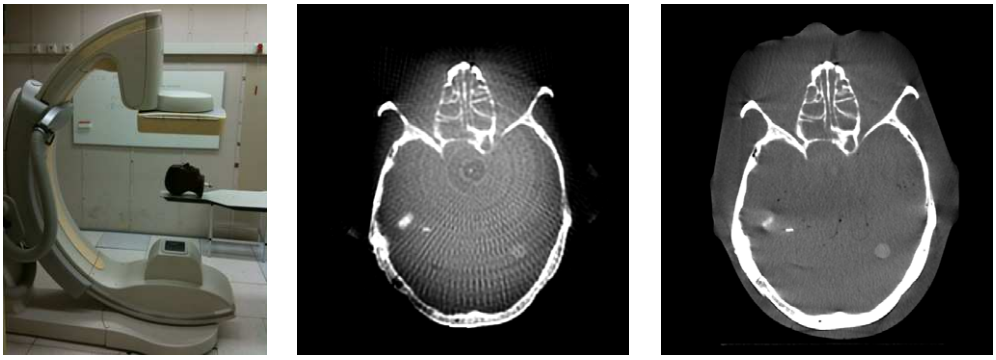

(a) (b) (c)

Figure 7. (a) The head phantom being scanned by a C-arm x-ray system. (b) A slice from the 3DRA reconstruction of the head phantom. (c) A slice from the cone-beam CT reconstruction of the head phantom.

The registration misalignment was further investigated using real clinical data. Since a ground truth transformation is not available for such data, we used the approach proposed by Woods *et al* (1998). Hereby, three datasets $\{A, B, C\}$ are available per patient that are all rigidly registered to each other. Ideally, multiplying the resulting registration matrices should deliver the identity matrix: $M_{AB} \cdot M_{BC} \cdot M_{CA} = I$. The discrepancies of the product from the identity matrix can be used as an indication of the accuracy of the registration approach though it cannot be pinpointed to any individual registration. We applied this method to five patients with one 3DRA reconstruction and two MR datasets each, whereby the registration was initialized by using the orientation information in the DICOM header and putting the origin in the center of the datasets. This delivered an average absolute translational discrepancy of 1.54 mm ($\sigma = 0.30$, min $= 1.21$, max $= 2.00$), and an average absolute rotational discrepancy of 0.68° ($\sigma = 0.26$, min $= 0.30$, max $= 0.94$). The isotropic voxel size for the 3DRA datasets varied from 0.35 to 0.48 mm. The pixel size of the MR slices varied from 0.42 to 0.76 mm, and the slice distance varied from 1.0 to 2.0 mm. Overall, it has been observed that the discrepancies in the product matrix are equal or less than the slice distance of the MR datasets.

3.3. Capture range

In order to validate the robustness and applicability of our multimodality registration approach in the clinical practice, we investigated the capture range of the mutual information-based automatic registration algorithm, using clinical data. In this context we defined the capture range as the extent of the parameter search space that can serve as the start position for the optimizer and still evolves to a correct spatial transformation between the datasets. If this extent is too small, the manual pre-registration becomes too cumbersome and time-consuming to be performed during an intervention.

To establish the range of the search space where the algorithm behaves robustly, we made the following assumption: if a registration process, started from a translation in a certain direction, evolves to the gold standard transformation, each registration attempt from a smaller translation in the same direction is also assumed to lead to the gold standard transformation, i.e. the capture range is convex without any holes. Though this assumption is a simplification of the real capture range, it allows us to investigate the capture range within reasonable time.

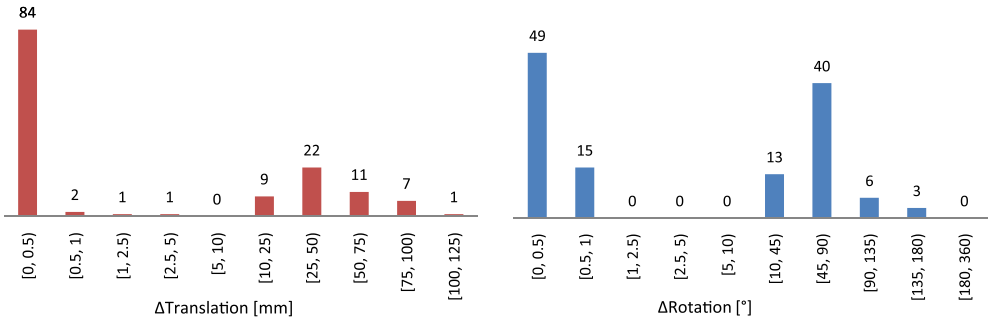

Figure 8. The absolute translational and rotational difference between a registration result and the gold standard transformation is investigated for a 3DRA-MR dataset pair. The bars in the chart show the amount of registration attempts that delivered a delta within the interval given below the bar. Note that the intervals on the left side of the graphs are smaller.

Also it has been observed that non-convexity mainly manifests itself at the borders of the capture range. As a result the non-convexity errors average out when a large number of measurements are taken.

Based on this assumption, the robust translation extent was determined, using an approach similar to a binary search (Knuth 1997). A gold standard transformation established by an expert was applied to the datasets, and one dataset was translated in a certain direction $\vec{d}$. If performing the registration process indeed leads to the gold standard transformation, the process was repeated with the translation vector doubled. If not, the translation vector was halved. A registration attempt was considered to be successful when all the components of the rotation matrix found by the registration differed less than a particular δ_R from the gold standard (we used $\delta_R = 0.05$), and the translation differed less than δ_T (we used $\delta_T = 1.0$ mm). Hereby, we rely on the fact that an erroneous registration typically leads to a matrix that significantly differs from a successful registration, as is illustrated in figure 8. Erroneous registrations are caused by the Powell optimization algorithm getting stuck in a local optimum. This usually only happens when the search space parameters are not close to the global optimum.

The iterative search was continued until a bounding interval (b_1, b_2), with $b_1 < b_2$, was found, whereby a translation of b_1 still was within the capture extent, and b_2 not. Then, iteratively a new limit $b = (b_1 + b_2)/2$ was tested. If a registration started from a translation with vector $b \cdot \vec{d}$ evolved to the gold standard transformation, b was within the capture range, and b_1 was set to b for the next iteration. Otherwise b_2 was set to b. In this way, the accuracy of the boundary of the capture range was doubled (the uncertainty was halved) in every iteration. The search was pursued until the boundary of the capture range was found with an accuracy of 5 mm. Using this method, the robust translation range was determined for every patient in 14 distinct directions (see figure 9). A similar scheme was used to determine the robust rotation extent around the x-, y- and z-axes in both directions. The robust rotation range was determined with a precision of 1°.

The capture range with respect to translation and rotation were determined for dataset pairs obtained from 17 patients: 7 patients with a 3DRA-CT dataset pair and 10 patients with a 3DRA-MR pair. 88% of the CT datasets can be registered correctly when the registration process is started within 30 mm translation to the gold standard transformation with the 3DRA dataset, see figure 10. 67% manage to robustly register within 50 mm translation. 88% of the CT datasets can still be registered correctly to the 3DRA dataset when the initial rotation

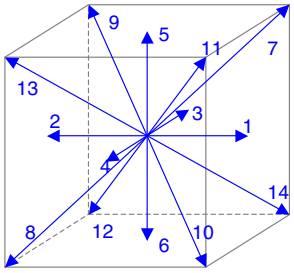

Figure 9. The translation of the datasets was tested in all 14 depicted directions.

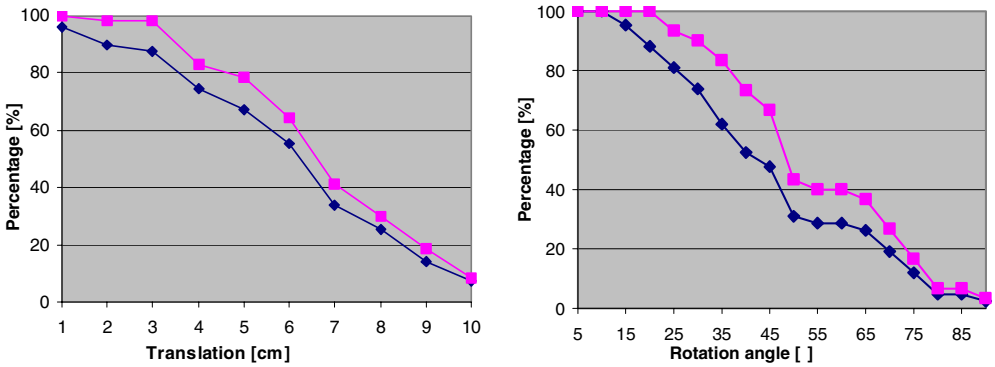

Figure 10. The percentage of 3DRA-CT dataset pairs that can be registered correctly for a given initial translation (left) or rotation (right). The upper line shows the results if the two most difficult to register CT datasets not taken into account, which provided only a limited field of view. The lower line indicates the results for all patients.

is 20° with respect to the gold standard, and 74% when the rotation is 30°. The extent of the capture range amounted on average 63.12 mm ($\sigma = 30.82$, min $= 5.96$, max $= 204.56$) for the translational component, and 40.08° ($\sigma = 21.62$, min $= 13.78$, max $= 91.34$) for the rotational component. The results we obtained are comparable to the ones published by Stancanello *et al* (2004).

The results for the ten 3DRA-MR dataset pairs are shown in figure 11. 80% of the MR datasets can be registered successfully when the initial translation is within 15 mm of the gold standard, and 84% yield correct results when the registration is started within 20° rotation. The extent of the capture range amounted on average 26.65 mm ($\sigma = 13.96$, min $= 5.78$, max $=$ 90.16) for the translational component, and 33.51° ($\sigma = 15.75$, min $= 6.71$, max $= 100.72$) for the rotational component.

3.4. Computation times

The pre-interventional steps consist of the 3DRA acquisition, the 3D–3D multimodal registration and the segmentation and mesh extraction of the vessels in the 3DRA dataset. The 3DRA acquisition and reconstruction take combined about 16 s. The linearly interpolated resampling of the floating dataset in the mutual information-driven registration of the multimodality data and the 3DRA data is performed on the graphics processing unit (GPU),

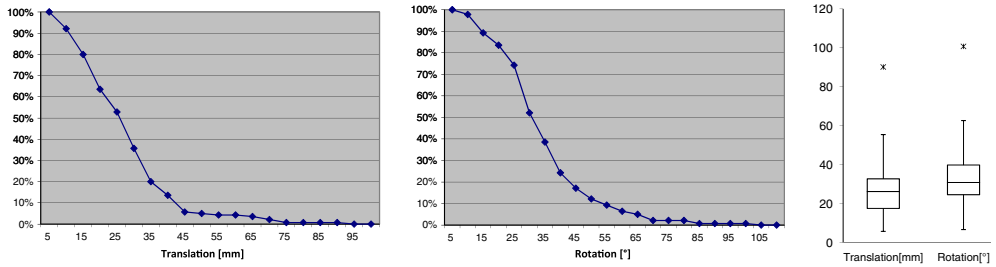

Figure 11. The percentage of 3DRA-MR dataset pairs that can be registered correctly for a given initial translation (left) or rotation (middle). The boxplots show the distribution of the capture range extents and their median.

and as a result the registration process can be executed in less than 8 s (Teßmann *et al* 2008, Shams and Barnes 2007).

The operations that have to be performed during the treatment are the 2D–3D machine-based registration and the fused visualization. The 2D–3D correspondence between the 3DRA dataset and the fluoroscopy image can be calculated in a mere 1.5 μs, and thus can be done in real time when the geometry sensor values change. The fused visualization, consisting of a mesh extracted from a 256^3 voxels 3DRA dataset, a volume-rendered slab from a $256^2 \times 198$ voxels CT dataset and the fluoroscopy image stream, can be displayed at an average frame rate of 38 frames s^{-1} (26 ms per frame). All measurements were performed on a Intel Xeon 3.6 GHz machine with 2 GB of memory, and an nVidia QuadroFX 3400 graphics card with 256 MB of memory.

4. Discussion

Being able to see the live fluoroscopy image within the context of the 3D vasculature and soft-tissue information is of great clinical relevance. The combination of the fluoroscopy image with the 3DRA vessel tree adds value, since the guide wire and the catheter position can be located with respect to the vessel tree without additional contrast injection, while the C-arm position and the x-ray SID can be altered freely. Even during rotations of the C-arm, the machine-based 2D–3D registration will always be up to date. The clinical interest of this so-called 3D-roadmapping has been described by Söderman *et al* (2005). The additional visualization of the soft-tissue data, allows correlating the position of the guide wire and catheter to anatomical information and pathologies which are only visible in the soft-tissue data (see figure 12). The fact that this information is available in real time makes it especially suitable for navigation. Phantom studies have shown that fused data can also increase the accuracy of vessel diameter measurements (Boussion *et al* 2004) and improve the visibility of microstents (Richter *et al* 2009).

Performing image registration of large 3D datasets during an interventional treatment poses a number of additional constraints on the registration method. Especially, the calculation times of the algorithms have to be limited, since they have to be carried out during the intervention. As we have shown in section 3.4, the computation times of the described algorithms are very modest. The pre-interventional steps only need a few seconds to be computed, and the live roadmapping steps with a latency of less than 30 ms are considered to be real time. Another aspect that is essential for image-guided treatment is accuracy. The tests with the cone-beam CT data as well as the real world MR data suggest that sub-voxel accuracy

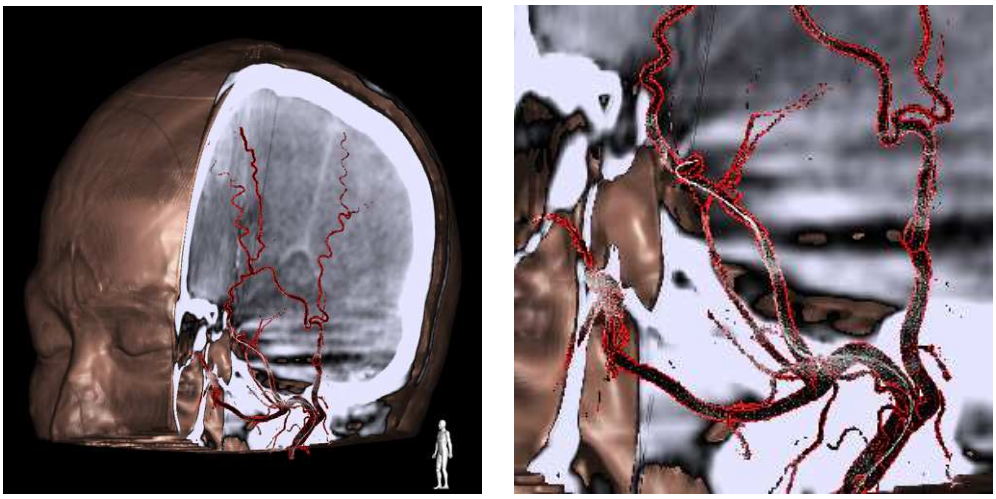

(a) (b)

Figure 12. (a) A quarter is cut out of a soft-tissue dataset, while the 3DRA vessels are overlayed with the live fluoroscopy information; (b) a zoomed fragment of the left image, showing the micro guide wire.

could be reached with the 3D–3D registration. In our case, the voxel size of 1 mm^3 for the used 3DRA reconstruction delivered an average residual registration error of 0.515 mm. The imprecision of the 2D–3D registration proved to be less than 0.2 mm in our experiments. The final aspect that was investigated in this study is the robustness of the image-based 3D–3D registration. For interventional use, it is important that the capture range of the registration algorithm is large enough, because there is no time for an elaborate manual initialization (a rough manual initialization is acceptable though). The majority of the registration attempts ($>80\%$) with CT data succeed when the initial translation is less than 35 mm and the rotation is less than 25°, compared to a gold standard transformation. For the MR data in our experiments the registration needed a finer initialization; 80% of the registration attempts succeed when the initial translation is less than 15 mm and the rotation is less than 20°.

After the automatic registration process has finished, the clinical user is asked to inspect the result and explicitly accept or reject it. In order to assess the proposed registration result, fused tomographic representations of the datasets are shown to the user, whereby the user can select the orientation (i.e. axial, lateral, caudal) and scroll through the slices. By looking at the common features in the datasets, it is possible to establish even modest mismatches in the range of 1–5 mm. As is shown in figure 8, it is usually not very difficult to identify an erroneous registration, since the mismatch is typically very large. In the case of a misregistration, the user can perform a finer manual initialization and restart the automatic registration process. Further possible sources of registration mismatches between the 3D data and the live 2D fluoroscopy images are patient motion and deformation of the anatomical structure during the course of the procedure (e.g. the deformation of vessels caused by the insertion of a catheter). Patient motion will cause a global mismatch of the guide wire and the 3D vessel lumen, whereas the deformation of vessels will lead to a local mismatch (see figure 13). It is up to the interventionalist to identify these issues, and take them into account. If the mismatch becomes too large, a new 3DRA dataset can be acquired and registered to the multimodal data.

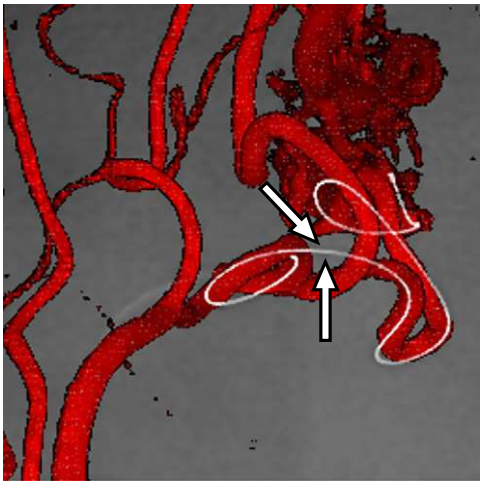

Figure 13. The insertion of intra-vascular devices (i.e. the catheter) can cause the vessels to deform, which can lead to a local mismatch between the 3D vessel lumen (acquired before the devices were inserted) and the intra-vascular devices as can be seen at the location of the arrows.

The morphological MR or CT dataset holds the soft-tissue structures relevant to the procedure as well as some pathological processes that may not be visible in the 3DRA or fluoroscopy data. The addition of soft-tissue visualization to the 3D-roadmapping technique brings extra information that may be important for the operator's decision-making and increase safety during the procedure as well as shorten the operating time. In embolizations of brain arteriovenous malformations (b-AVMs) or intracranial tumors using liquid adhesives or particles, the exact position of the catheter tip is crucial. The obvious goal is to embolize the pathological structures and avoid spilling over to the normal vessel supplying the normal brain tissue. The complicated vessel anatomy can in these situations be difficult to comprehend and the 3D multimodality roadmapping may in such instances prove to be of great value. The technique may also be of assistance for targeting areas of a b-AVM that are to be partially embolized thereby avoiding the so-called piece-meal embolization, as well as for avoiding high risk treatment close to eloquent areas of the brain (figure 14). The exact position for delivery is also important for intra-arterial delivery of other compounds, i.e. cytostatic agents for tumors, growth factors for stroke and degenerative brain disorders, a field that at the moment is largely developing and growing.

Clinical results have been described by Levitt *et al* (2011). They successfully combined pre-interventional CTA and MRA with real-time imaging at the time of angiography, and reported that the technique can reduce radiation and iodinated contrast exposure, and expands the application of angiographic technology in cerebrovascular and other neurosurgical diseases. Clinically relevant potential to lower contrast media use and a reduction of the risk of thrombo-embolic events is reported by Lin *et al* (2010), when the multimodality roadmapping method is used for navigation in areas ranging from the aortic arch level to the proximal internal carotid arteries. Gupta and Radaelli (2009) have described how the presented method can also be applied in transarterial chemoembolization (TACE). The fusion of the 3DRA with diagnostic CT or MR angiography enables valuable multimodal visualizations of feeding vessels and tumors. The 3D roadmapping, using the live 2D fluoroscopy, allows a smooth catheter placement into the feeding vessels. Spelle *et al* (2009) and Cooke *et al* (2010) have

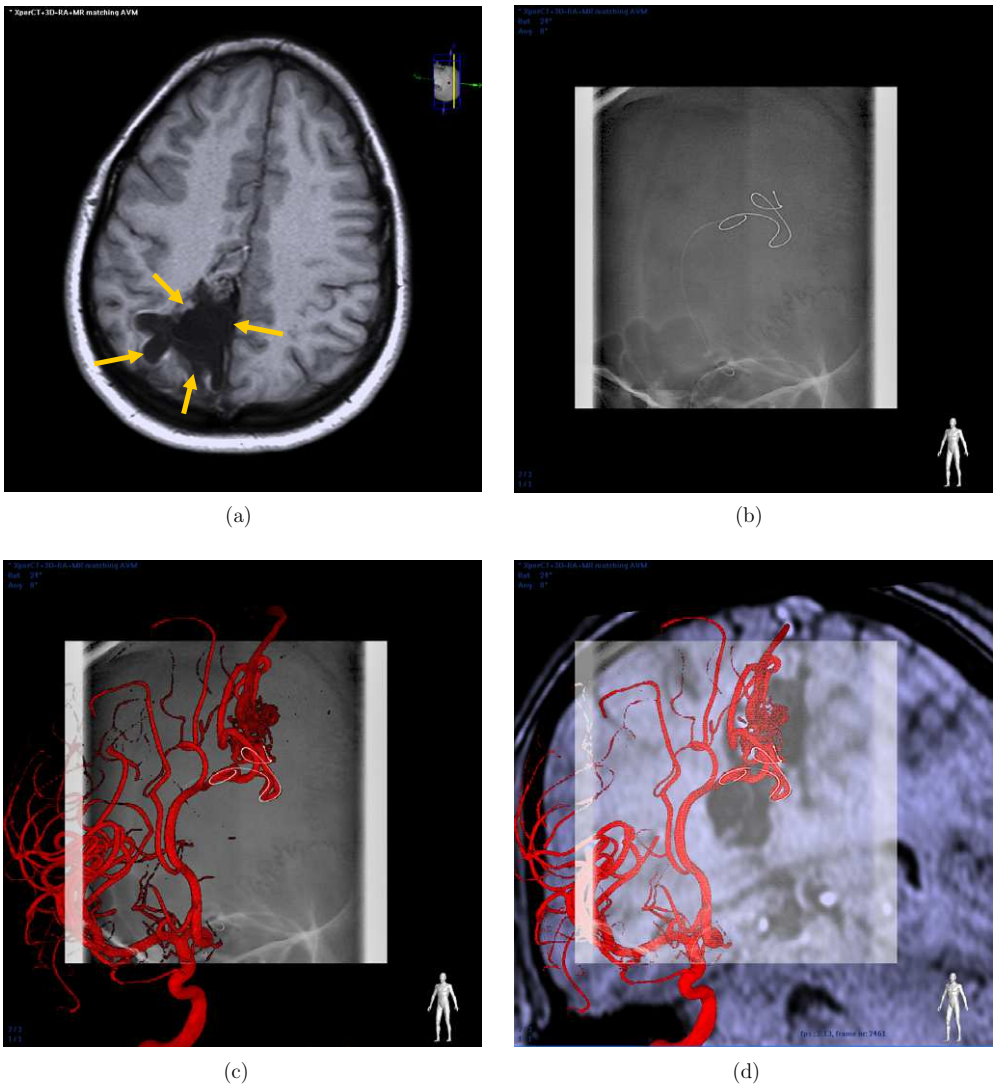

(a) (b)

(c) (d)

Figure 14. (a) An MR image, showing an AVM and impacted brain tissue, indicated by the arrows, (b) the live fluoroscopy image without contrast medium shows the guide wire, but does not reveal its relation to the vasculature and the soft-tissue, (c) the fluoroscopy image mixed with the vessel tree from the 3DRA dataset adds the vascular context to the live data, (d) the fluoroscopy image, the 3DRA vasculature and a slab from the MR data. The MR slab is positioned parallel to the view port at the guide wire tip.

reported using the 3D multimodal fused roadmapping when navigating percutaneous needle punctures to embolize a skull base glomus tumor and an intraorbital mass, respectively.

5. Conclusions

The scope of this paper is concerned with the validation of fusing real-time fluoroscopy, 3DRA data and soft-tissue data into a combined image. The steps necessary to achieve this

data fusion have been described. To bring the pre-operative data in the coordinate frame of the C-arm equipment, a fast automatic image-based registration of the 3DRA dataset and the soft-tissue dataset has been developed. The machine-based registration between the 2D fluoroscopy image and the 3DRA data only depends on the geometry incidence angles, the x-ray SID and the calibration data. It can be readily calculated in real time.

In this paper, we have addressed the accuracy, robustness and computation time of the various aspects of the presented methods. The investigations of the precision of the registration yielded an average residual error of 0.515 mm for the 3D–3D registration and less than 0.2 mm for the live 2D–3D registration. The accuracy of the composition of both steps is in the same range as the image content-based 2D–3D registration algorithms (Bullitt *et al* 1999, Byrne *et al* 2004), but the computation of the intra-procedural part is much faster. The robustness of the image-based 3D–3D registration was examined for the registration of 3DRA with CT data (capture range of 35 mm and 25° for >80% of the data), and 3DRA with MR data (capture range of 15 mm and 20° for >80% of the data). The speed of the algorithms is regarded as very satisfactory for the usage during clinical treatment.

Furthermore, the usage of the presented methods within neuro-endovascular procedures has been briefly discussed. The combination of the fluoroscopic image with the 3DRA vessel tree, known as 3D roadmapping, offers the advantage that the spatial relationship between the endovascular device and the surrounding vessel morphology can be determined, without additional contrast injection, while the position of the C-arm geometry can be altered freely. The strength of the described approach lies in the possibility of correlating the position of endovascular devices and pre-interventional soft-tissue image data accurately and in real time. The clinical feedback has been encouraging; the 3D roadmapping technique is considered a valuable method for accurate navigation and helps to reduce x-ray dose and use of a harmful iodine contrast agent (Söderman *et al* 2005, Gupta and Radaelli 2009, Lin *et al* 2010).

A possible disadvantage of the present method is the fact that patient motion will render the 2D–3D registration to be invalid. Therefore, future work could combine machine-based registration with image-based registration to correct for patient motion.

References

Baert S A M, Penney G P, van Walsum T and Niessen W J 2004 Precalibration versus 2D–3D registration for 3D guide wire display in endovascular interventions *MICCAI '04* pp 577–84

Bender F, Groher M, Khamene A, Wein W, Heibel T H and Navab N 2008 3D dynamic roadmapping for abdominal catheterizations *MICCAI '08* pp 668–75

Boussion N, Soulez G, Guise J A D, Daronat M, Qin Z and Cloutier G 2004 Geometrical accuracy and fusion of multimodal vascular images: a phantom study *Med. Phys.* **31** 1434–43

Brigger P, Müller F, Illgner K and Unser M 1999 Centered pyramids *IEEE Trans. Image Process.* **8** 1254–64

Bullitt E, Liu A, Aylward S R, Coffey C, Stone J, Mukherji S K, Muller K E and Pizer S M 1999 Registration of 3d cerebral vessels with 2d digital angiograms: clinical evaluation *Acad. Radiol.* **6** 539–46

Byrne J V, Colominas C, Hipwell J, Cox T, Noble J A, Penney G P and Hawkes D J 2004 Assessment of a technique for 2d–3d registration of cerebral intra-arterial angiography *Br. J. Radiol.* **77** 123–8

Cañero C, Nofrerías E, Mauri J and Radeva P 2002 Modelling the acquisition geometry of a C-arm angiography system for 3D reconstruction *CCIA* pp 322–35

Cooke D L, Levitt M, Kim L J, Hallam D K and Ghodke B 2010 Intraorbital access using fluoroscopic flat panel detector CT navigation and three-dimensional MRI overlay *J. NeuroIntervent. Surg.* **2** 249–51

Fahrig R and Holdsworth D W 2000 Three-dimensional computed tomographic reconstruction using a C-arm mounted XRII: image-based correction of gantry motion nonidealities *Med. Phys.* **27** 30–38

George A K, Sonmez M, Lederman R J and Faranesh A Z 2011 Robust automatic rigid registration of MRI and x-ray using external fiducial markers for XFM-guided interventional procedures *Med. Phys.* **38** 125–41

Gorges S, Kerrien E, Berger M-O, Pescatore J, Anxionnat R and Picard L 2005 Model of a vascular C-arm for 3D augmented fluoroscopy in interventional radiology *MICCAI '05* pp 214–22

Gorges S, Kerrien E, Berger M-O, Pescatore J, Trousset Y, Anxionnat R, Bracard S and Picard L 2006 3D augmented fluoroscopy in interventional neuroradiology: precision assessment and first evaluation on clinical cases *MICCAI Workshop AMI-ARCS '06* pp 1–10

Groher M, Jakobs T F, Padoy N and Navab N 2007 Planning and intraoperative visualization of liver catheterizations: new CTA protocol and 2D–3D registration method *Acad. Radiol.* **14** 1325–40

Gupta A and Radaelli A G 2009 Live 3D guidance in endovascular procedures *Endovascular Today* July 2009 pp 28–40

Hartley R and Zisserman A 2000 *Multiple View Geometry in Computer Vision* (Cambridge: Cambridge University Press)

Jain A K, Mustafa T, Zhou Y, Chirikjian G S and Fichtinger G 2005 FTRAC—a robust fluoroscope tracking fiducial *Med. Phys.* **32** 3185–98

Jomier J, Bullitt E, van Horn M, Pathak C and Aylward S R 2006 3D/2D model-to-image registration applied to TIPS surgery *MICCAI '06* pp 662–9

Kalender W A and Kyriakou Y 2007 Flat-detector computed tomography (FD-CT) *Eur. Radiol.* **17** 2767–79

Kerrien E, Vaillant R, Launay L, Berger M-O, Maurincomme E and Picard L 1998 Machine precision assessment for 3D/2D digital subtracted angiography images registration *SPIE Medical Imaging* pp 39–49

Kita Y, Wilson D L and Noble J A 1998 Real-time registration of 3D cerebral vessels to x-ray angiogram *MICCAI '98 (London)* (Berlin: Springer) pp 1125–33

Knuth D E 1997 *The Art of Computer Programming. Volume 3: Sorting and Searching (Section 6.2.1: Searching an Ordered Table)* (Reading, MA: Addison-Wesley)

Koppe R, Klotz E, Op de Beek J and Aerts H 1995 3D vessel reconstruction based on rotational angiography *Proc. CAR (Berlin)* pp 101–7

Levitt M R, Ghodke B V, Cooke D L, Hallam D K, Kim L J and Sekhar L N 2011 Endovascular procedures with CTA and MRA roadmapping *J. Neuroimaging* **21** 259–62

Lin C-J, Blanc R, Clarençon F, Piotin M, Spelle L, Guillermic J and Moret J 2010 Overlying fluoroscopy and preacquired CT angiography for road-mapping in cerebral angiography *Am. J. Neuroradiol.* **31** 494–5

Maes F, Collignon A, Vandermeulen D, Marchal G and Suetens P 1997 Multimodality image registration by maximization of mutual information *IEEE Trans. Med. Imaging* **16** 187–98

Maintz J B A and Viergever M A 1998 A survey of medical image registration *Med. Image Anal.* **2** 1–36

McLaughlin R A, Hipwell J, Hawkes D J, Noble J A, Byrne J V and Cox T C 2005 A comparison of a similarity-based and feature-based 2-D–3-D registration method for neurointerventional use *IEEE Trans. Med. Imaging* **24** 1058–66

Noordhoek N J, van de Haar P G and Timmer J 2006 Direct comparison of commercially available C-arm CT to multislice CT image quality *Proc. RSNA (Chicago, IL)* p 377

Penney G P, Batchelor P G, Hill D L G, Hawkes D J and Weese J 2001 Validation of a two- to three-dimensional registration algorithm for aligning preoperative CT images and intraoperative fluoroscopy images *Med. Phys.* **28** 1024–31

Peters T M, Clark J A, Olivier A, Marchand E P, Mawko G, Dieumegarde M, Muresan L V and Ethier R 1986 Integrated stereotaxic imaging with CT, MR imaging, and digital subtraction angiography *Med. Phys.* **161** 821–6

Press W H, Teukolsky S A, Vetterling W T and Flannery B P 1992 *Numerical Recipes in C: The Art of Scientific Computing* (New York: Cambridge University Press)

Richter G, Pfister M, Struffert T, Engelhorn T, Doelken M, Spiegel M, Hornegger J and Doerfler A 2009 Technical feasibility of 2D–3D coregistration for visualization of self-expandable microstents to facilitate coil embolization of broad-based intracranial aneurysms: an *in vitro* study *Neuroradiology* **51** 851–4

Rougée A, Picard C L, Trousset Y L and Ponchut C 1993 Geometrical calibration for 3D x-ray imaging *Proc. SPIE* **1897** 161–9

Ruijters D, Babic D, Homan R, Mielekamp P, ter Haar Romeny B M and Suetens P 2009 Real-time integration of 3-D multimodality data in interventional neuroangiography *J. Electron. Imaging* **18** 033014

Shams R and Barnes N 2007 Speeding up mutual information computation using NVIDIA CUDA hardware *Proc. Digital Image Computing: Techniques and Applications (DICTA) (Washington, DC)* (Los Alamitos, CA: IEEE Computer Society Press) pp 555–60

Söderman M, Babic D, Homan R and Andersson T 2005 3D roadmap in neuroangiography: technique and clinical interest *Neuroradiology* **47** 735–40

Spelle L, Ruijters D, Babic D, Homan R, Mielekamp P, Guillermic J and Moret J 2009 First clinical experience in applying XperGuide in embolization of jugular paragangliomas by direct intratumoral puncture *Int. J. Comput. Assist. Radiol. Surg.* **4** 527–33

Stancanello J, Cavedon C, Francescon P, Cerveri P, Ferrigno G, Colombo F and Perini S 2004 Development and validation of a CT-3D rotational angiography registration method for AVM radiosurgery *Med. Phys.* **31** 1363–71

Stancanello J, Cavedon C, Francescon P, Cerveri P, Ferrigno G, Causin F and Colombo F 2005 CT-3D rotational angiography automatic registration: a sensitivity analysis *Med. Biol. Eng. Comput.* **43** 667–71

Teßmann M, Eisenacher C, Enders F, Stamminger M and Hastreiter P 2008 GPU accelerated normalized mutual information and B-spline transformation *Proc. Eurographics Workshop on Visual Computing for Biomedicine (EG VCBM)* pp 117–24

Tomaževič D, Likar B and Pernuš F 2006 3-D/2-D registration by integrating 2-D information in 3-D *IEEE Trans. Med. Imaging* **25** 17–27

Turgeon G-A, Lehmann G, Drangova M, Holdsworth D and Peters T 2005 2D–3D registration of coronary angiograms for cardiac procedure planning *Med. Phys.* **32** 3737–49

van de Kraats E B, Penney G P, Tomaževič D, van Walsum T and Niessen W J 2005 Standardized evaluation methodology for 2D–3D registration *IEEE Trans. Med. Imaging* **24** 1177–90

Weese J, Penney G P, Desmedt P, Buzug T M, Hill D L G and Hawkes D J 1997 Voxel-based 2-D/3-D registration of fluoroscopy images and CT scans for image-guided surgery *IEEE Trans. Inf. Technol. Biomed.* **1** 284–93

Woods R P, Grafton S T, Holmes C J, Cherry S R and Mazziotta J C 1998 Automated image registration: I. General methods and intrasubject, intramodality validation *J. Comput. Assist. Tomogr.* **22** 139–52